

Numerical study of the gravitational shock wave inside a spherical charged black hole

Ehud Eilon and Amos Ori

May 6, 2021

Department of Physics,

Technion - Israel Institute of Technology,

Haifa 3200003, Israel

Abstract

We numerically investigate the interior of a four-dimensional, asymptotically flat, spherically symmetric charged black hole perturbed by a scalar field Φ . Previous study by Marolf and Ori indicated that late infalling observers will encounter an effective shock wave as they approach the left portion of the inner horizon. This shock manifests itself as a sudden change in the values of various fields, within a tremendously short interval of proper time τ of the infalling observers. We confirm this prediction numerically for both test and self-gravitating scalar field perturbations. In both cases we demonstrate the effective shock in the scalar field by exploring $\Phi(\tau)$ along a family of infalling timelike geodesics. In the self-gravitating case we also demonstrate the shock in the area coordinate r by exploring $r(\tau)$. We confirm the theoretical prediction concerning the shock sharpening rate, which is exponential in the time of infall into the black hole. In addition we numerically probe the early stages of shock formation. We also employ a family of null (rather than timelike) ingoing geodesics to probe the shock in r . We use a finite-difference numerical code with double-null coordinates combined with a recently developed adaptive gauge method in order to solve the (Einstein + scalar) field equations and to evolve the spacetime (and scalar field) — from the region outside the black hole down to the vicinity of the Cauchy horizon and the spacelike $r = 0$ singularity.

1 INTRODUCTION

Background: The inner structure of classical black holes (BHs) has been a subject of continuous investigation over the last half century. The interior of a Reissner-Nordström (RN) or Kerr BH (representing a charged or spinning BH respectively) is drastically different from that of a Schwarzschild BH. In the latter there is a fatal, destructive, spacelike singularity at $r = 0$, and all infalling observers inevitably crash at that singularity. By contrast, in the RN and Kerr solutions there is an inner horizon (IH) at finite r , instead of a spacelike singularity. An $r = 0$ singularity still exists in these two solutions, but it is timelike rather than spacelike, it is located beyond the inner horizon, and infalling geodesics generically avoid it (unlike the Schwarzschild case). Figure 1a displays the Penrose diagram of the eternal (analytically extended) RN spacetime. The Kerr case is basically similar (at least with regards to the aspects considered in this paper).¹

The IH in the RN and Kerr spacetimes also serves as a *Cauchy horizon* (CH), a null hypersurface which marks the future boundary of physical predictability (for initial data specified in the external world). Note that in an RN or Kerr BH there are two distinct inner-horizon hypersurfaces (see Fig. 1a), namely a left-going arm and a right-going one. In the case of eternal BH, the CH contains both IH arms (up to their bifurcation point b). This is directly related to the presence of two external asymptotic universes, W and W' . However, in the case of a non-eternal charged BH produced in spherical charged collapse (see Fig. 1b), the left-right symmetry breaks, and the asymptotic universe W' no longer exists. In this case only the left-going arm of the IH is a CH. The other IH arm seems to have no special causal role in the charged-BH spacetime. The situation with spinning BHs is basically similar: In the eternal Kerr spacetime the CH contains both arms of the IH; but in the non-eternal, spinning-collapse case (with asymptotically-Kerr exterior) only the left-going arm belongs to the CH.

2

¹ Certain differences and additional subtleties arise in the spacetime diagram of Kerr, but they all occur beyond the IH and are hence not so relevant to the present paper. (To mention two such differences: The $r = 0$ singularity in Kerr is actually a *ring*, and at its “other side(s)” there is an additional external asymptotic universe, of a different type.)

²In the case of spherical charged collapse, the spherically-symmetric electrovac exterior will uniquely be described by the RN geometry. But in the spinning analog, the vacuum exterior will generically fail to be Kerr. Indeed, at late time the geometry should approach a Kerr BH (the “no hair” principle). However, in this case the CH will become a weak curvature singularity (in contrast with the regular CH in the cases of pure Kerr and RN geometries, and in the case of unperturbed spherical charged collapse.) We shortly discuss this type of weakly-singular CH.

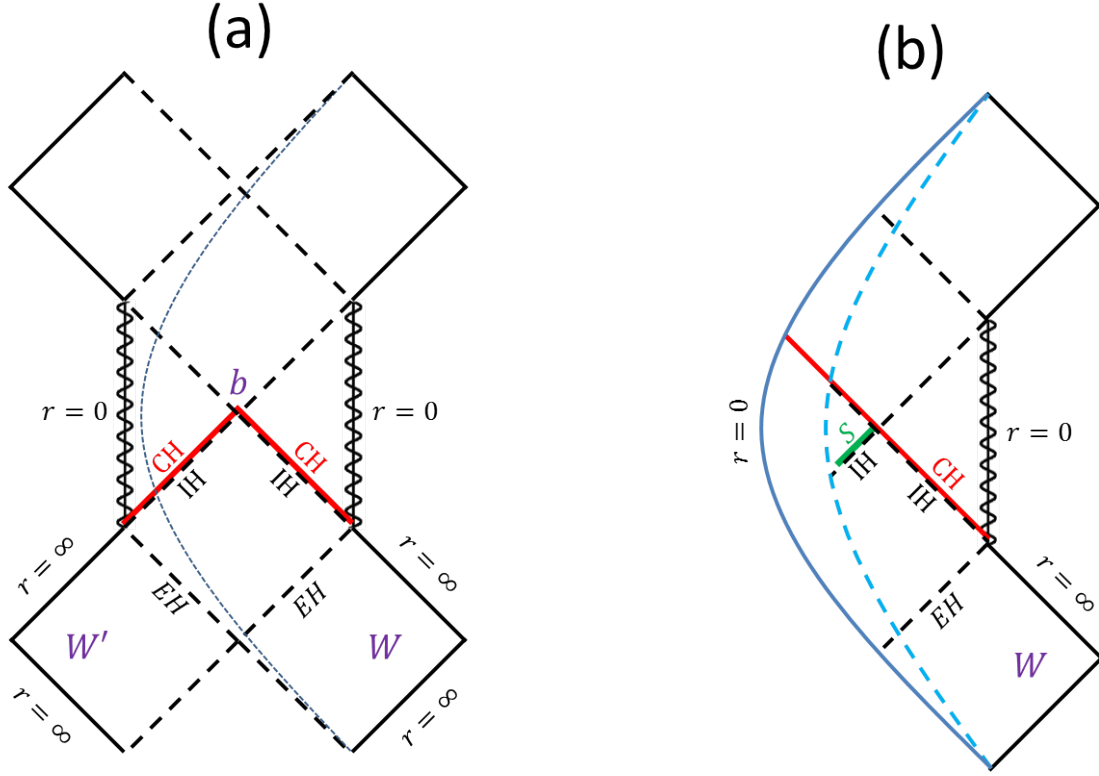


Figure 1: Penrose diagrams of the eternal RN spacetime (panel a) and a charged BH produced by thin-shell collapse (panel b). In the latter, the geometry is RN outside the collapsing shell (the dashed blue curve) and Minkowski inside the shell, with a regular center at $r = 0$ (the solid blue curve). In both panels, solid black diagonal lines denote null infinity; solid red diagonal lines denote the Cauchy horizon (CH). Dashed black diagonal lines denote the event horizon (EH) and the inner horizon (IH); the latter partly overlaps with the CH in both cases. Wavy vertical lines denote the timelike $r = 0$ singularity of RN. The eternal RN spacetime in panel a includes a twin set of asymptotically flat universes, W and W' . This panel also shows a typical timelike geodesic (the dotted blue curve) which falls into the BH from the external universe W , avoids the timelike $r = 0$ singularity, then emerges from a white hole and arrives at a future external universe (isometric to W). The spacetime diagram in panel a is right-left symmetric; and the CH has two arms which intersect at a bifurcation point “b”. The charged-collapse diagram in panel b is not right-left symmetric, and the CH includes only one arm of the IH (the left-going one). When the collapsing charged BH of panel b is generically perturbed, a null weak singularity forms at the CH; and an effective shock develops along the solid green line denoted “S” (at the right-going IH).

In the late 1960s Penrose pointed out that the CH, in both RN and Kerr geometries, is a locus of infinite blue-shift. [1] He suggested that this diverging blue-shift would lead to divergent energy fluxes, and hence to a curvature singularity instead of a regular IH. Since then, many investigations were made in an attempt to analyze the effect of perturbations on the internal structure of the (charged or spinning) BH — and particularly at the CH. In order to simplify the analysis, most of these investigations [2, 3, 4, 5, 6, 7, 8, 9, 10, 11, 12, 13] were restricted to spherical charged BHs, because spherical symmetry drastically simplifies the structure of spacetime. Of particular importance were the works of Hiscock [3] and of Poisson and Israel [6, 7]: Hiscock considered an ingoing null fluid perturbation, and showed that a (non-scalar) null curvature singularity forms at

the CH. Poisson and Israel introduced the mass-inflation model, which contains two null fluids. They concluded that a scalar-curvature null singularity will form at the CH in this case, the so-called *mass-inflation singularity*. Ori [8] then found (using a simplified shell model) that the mass-inflation singularity is actually weak (in Tipler’s [14] sense; see also [15]), despite of its scalar-curvature character. Namely, the metric tensor approaches a finite (non-singular) limit at the CH; and extended objects will only experience finite (possibly small) tidal distortion on approaching the CH. Subsequently, several authors extended these studies to the case of a spherical charged BH perturbed by a self-gravitating scalar field. Numerical investigations [10, 11] revealed that in this case too, a weak null curvature singularity develops at the CH. In addition, the CH undergoes contraction due to crossing energy fluxes, and eventually it shrinks to zero area (namely $r = 0$). Various numerical simulations [10, 11, 12, 16] indicated that at this point of full contraction, the null CH meets a spacelike $r = 0$ singularity, as seen in Fig. 6 below. This basic picture, of a weak null singularity forming at the CH, was recently confirmed mathematically by Dafermos [17].

The non-spherical model of a rotating BH is of course much more realistic than its spherical-charged counterpart (as astrophysical BHs are presumably rotating but not significantly charged). Considering the case of a perturbed asymptotically-flat spinning BH, it was found [18] (based on nonlinear perturbation analysis) that the situation is similar in many respects to the case of perturbed spherical charged BHs discussed above: Owing to the infinite blue-shift of the infalling gravitational perturbations, a null weak scalar-curvature singularity develops at the CH in this case too. Later an independent analysis [19] yielded consistent results. Note a remarkable difference between the spinning and spherical-charged cases, though: In the spinning case the CH singularity turns out to be oscillatory [20], unlike the monotonic growth of curvature scalars in the mass-inflation singularity.

The accumulation of all these investigations, over the last few decades, led to a fairly clear and coherent picture: ³ Consider either a spinning or charged BH produced in gravitational collapse. A (null and weak) scalar-curvature singularity will generically develop at the CH, namely the *left-going* section of the IH. No such curvature singularity is expected to form at the latter’s right-going section — which, as mentioned above, is *not* a CH. [21]

Experience of infalling observers: Consider now a hypothetical observer who arrives a charged (or spinning) non-eternal BH a long time after the collapse, and decides to jump in. In view of the no-hair principle, the BH will look pretty much like RN (or Kerr), with only negligible deviations, perhaps even undetectable ones. This asymptotic RN metric will have a final mass and charge parameters M_f and Q_f , and hence outer and inner horizon radius $r_{\pm} = M_f \pm (M_f^2 - Q_f^2)^{1/2}$, where relativistic units $c = G = 1$ are used throughout the paper. (In the Kerr case, Q_f should be replaced by the asymptotic spin parameter a_f .) Once inside the BH, the observer will inevitably fall towards the IH, and its r value will monotonically decrease from r_+ to r_- . Throughout most of this journey from the EH to the IH, the deviations from the RN/Kerr metric are still negligible — and, ignoring these tiny deviations, the observer would have the same experience as moving in an exact RN/Kerr geometry. Assuming that the observer is equipped with a rocket, he can choose whether to reach $r = r_-$ at the right portion of the IH, or at its left portion. We shall refer to such observers as

³We point out, however, that several cardinal questions concerning the interior of classical BHs still remain open. Perhaps the most important one is, whether a spacelike singularity forms inside a generically-perturbed spinning BH.

right-fallers or *left-fallers*, respectively.⁴

Let's consider first the experience of a right-faller. The right portion of r_- is the CH, which, as was discussed above, is a locus of a curvature singularity. Throughout most of the travel from r_+ to r_- the observer will feel nothing but the background RN/Kerr curvature (which would be fairly mild for a supermassive BH), with only negligible deviations. Only when r becomes very close to r_- , tidal forces will start to grow very rapidly, and will diverge at the CH itself. (Although, the integrated deformation will be finite even at the CH itself⁵.) This is the basic picture that emerges from the collection of the various investigations over the last few decades.

But what will be the experience of a left-faller? The above-mentioned investigations haven't directly addressed this question, except that they collectively made clear one important fact: Since the BH is non-eternal (it has presumably been produced in gravitational collapse), the left portion of $r = r_-$ is *not* a locus of divergent curvature (because it is not a CH); hence, in principle spacetime should be perfectly smooth on crossing this portion of the IH.

Of course, the left-faller should expect very serious troubles to come later on; for example, a strong spacelike singularity may exist in the perturbed spacetime, say at $r = 0$. But this should happen somewhere at $r < r_-$, namely sometime *after* crossing $r = r_-$. Exactly where the fatal tidal forces will be encountered, this might depend on the details of the BH model. These considerations might lead to the impression that the experience of a left-faller is rather non-universal and hard to predict, and in particular it might be sensitive to various details of the collapse scenario.

Effective shock wave: Despite of the above, Marolf and Ori (MO) [22] recently found that the experience of late left-fallers, when recorded as a function of their own proper time τ , does exhibit an interesting universal pattern — a shock-like behavior. Namely, various measurable quantities undergo abrupt changes as $r = r_-$ is approached. For any individual left-faller, this change actually takes a finite lapse of proper time $\Delta\tau$ (in line with the aforementioned regularity of spacetime at the left section of $r = r_-$). However, this finite width $\Delta\tau$ rapidly decreases with delaying the moment of infall into the BH. Based on simple theoretical arguments, MO concluded that $\Delta\tau \propto e^{-\kappa_- \Delta t}$, where κ_- is the IH surface gravity, and Δt is (roughly speaking) the time lapse from BH formation to the moment of jumping in, expressed in terms of asymptotic time coordinate t in the external universe. (Later we shall re-express this exponential relation more precisely in terms of Eddington's advanced time coordinate v_e .) For a left-faller which jumps in after a time delay Δt of, say, a few tens or hundreds times the BH mass M , the width scale $\Delta\tau$ will be tremendously smaller than Planck time, by many orders of magnitude; so small that it is not clear if it could be resolved by any physical probe. We therefore refer to this rapid change in the various measurable quantities as an “effective discontinuity”, or *effective shock wave*, which forms at the left-arm IH.

The analysis by MO addressed both charged and spinning BHs. The effective shock wave shows

⁴To avoid confusions that may potentially be associated with this “right-left” terminology, we emphasize that the *right* (or *left*) portion of $r = r_-$ is *left-going* (or *right-going*); See Fig. 1a. Note also that in the RN case, an infalling geodesic will always take the observer directly to the left portion of $r = r_-$; he would have to turn on his rocket in order to reach the right portion. However in the Kerr case geodesics reach either the left or right portions.

⁵Recall that, since the CH singularity is weak, the integrated tidal deformation is finite (and non-destructive) even at the singularity; furthermore, for sufficiently late infall time, the overall singularity-induced deformation may be arbitrarily small. Nevertheless, the tidal force itself will always diverge at the singular CH.

itself in various quantities, e.g. metric functions as well as other perturbing fields. In this paper we consider the model of a spherical charged BH perturbed by a scalar field, and focus on the shock formation in two quantities: the perturbing scalar field, and the area coordinate r — which is essentially a (square root of the) metric function for the angular sector.

Numerical verification: The analysis in Ref. [22] was carried entirely analytically, by focusing on the late-time behavior of the relevant perturbation fields inside the BH. The investigation was thus heavily based on perturbation analysis, although in certain points it also involved some qualitative considerations concerning the dynamics beyond the small-perturbation domain.

As an example, consider the shock in r : It involves a sudden decrease of r from r_- towards $r = 0$, within an extremely small $\Delta\tau$ (see Sec. 5.3 below). This clearly involves a large deviation of $r(\tau)$ from its smooth RN counterpart. This situation is thus beyond the domain of validity of perturbation analysis. Hence it would be worthwhile to confirm this shock behavior by independent, non-perturbative, analysis. Another limitation of the analysis by MO was that it was mostly restricted to the late-time domain, and therefore was incapable of resolving the earlier times where the shock just starts to develop (namely, the domain of small-moderate Δt values at which $\Delta\tau$ starts its decrease from its initial $\mathcal{O}(M)$ value to its later $\ll M$ values).

We therefore found it important to carry detailed numerical simulations for exploring the shock phenomenon inside the BH. Specifically we were motivated by several goals and objectives, including: (i) verifying the very existence of the effective shock, (ii) verifying the shock’s exponential sharpening rate, (iii) exploring the early phase of shock formation, and (iv) exploring the well-developed shock in r , all the way down to $r \ll r_-$ values (which, as pointed out above, are out of the perturbative domain).

To this end, we carried a numerical analysis of a spherical charged BH perturbed by either a test scalar field or a self-gravitating one. We used the double-null numerical code [16] which we recently developed for that purpose. We study the effective shock in the scalar field and (in the self-gravitating case) also in the area coordinate r . We explore both the early shock formation and the later domain of fully developed shock. In the latter domain, we also measure the rate of shock sharpening, and compare it to MO’s prediction in [22]. We found nice agreement between this prediction and our numerical results, concerning both the very existence of the shock and its rate of sharpening.

The paper is organized as follows: We formulate the physical problem in terms of the unknown functions, the field equations, and the set-up of initial conditions in Sec. 2; we summarize our numerical algorithm in Sec. 3. Since we discussed both of these subjects extensively in our previous paper [16], here we only summarize them briefly. We then numerically analyze the case of a test scalar field perturbation on a prescribed RN background in Sec. 4. In particular, we demonstrate the formation of effective shock in the scalar field, and show that its development exhibits a continuous sharpening, in nice quantitative agreement with the prediction made by MO. The case of a self-gravitating scalar field perturbation on a spherical charged background is analyzed in Sec. 5, where we demonstrate the expected shock formation in both the scalar field and the metric function r . The rate of shock sharpening (for both the scalar field and r) is measured and compared to MO’s prediction. In addition, we also explore the shock in r as expressed in terms of the affine parameter

λ along null (rather than timelike) ingoing geodesics. We find that null geodesics provide an efficient tool for exploring the shock. Finally, we discuss our results and conclusions in Sec. 6.

2 PHYSICAL SYSTEM AND FIELD EQUATIONS

We explore the formation and development of the shock wave in two different physical scenarios: (i) Evolving *test scalar field* on a prescribed, static, RN background; and (ii) the evolution of a *self-gravitating scalar field* on a dynamical charged BH background.

In the first scenario the background metric is fully known, a-priori and analytically; in principle one could solve the scalar-field wave equation only, on the prescribed RN background. We found it more convenient, however, to numerically solve the Einstein equation as well — with electrovac initial data. The evolving metric then yields the RN solution (up to negligible numerical errors). This set-up allows more flexible switching between scenarios (i) and (ii), which in particular yields better debugging capabilities. Also, it allows easier handling of the gauge used for the background RN geometry — simply by dictating the gauge of the initial functions. As a consequence, the basic numerical setting of the self-gravitating system described in this section — namely simultaneous numerical solution of the Einstein and scalar-field equations — actually applies to the test-field case as well.⁶

The scalar field Φ is uncharged, massless, and minimally coupled, satisfying the standard wave equation $\square\Phi = 0$. The geometry is initially RN, but is subsequently perturbed by an ingoing pulse of scalar field (see below). The initial RN geometry has mass M_0 and charge Q . The line element may be expressed in double-null coordinates (u, v, θ, φ) (applicable to both the RN and perturbed geometries):

$$ds^2 = -e^{\sigma(u,v)} du dv + r(u, v)^2 d\Omega^2, \quad (1)$$

where $d\Omega^2 \equiv d\theta^2 + \sin^2\theta d\varphi^2$. Our three unknown functions are the scalar field $\Phi(u, v)$ and the metric functions $r(u, v)$ and $\sigma(u, v)$.

The general setup of our simulation, and the location of the numerical grid in the (would-be) RN background, are illustrated in Fig. 2. The scalar field perturbation is taken to be an ingoing initial pulse which propagates toward the BH, and is partly scattered and partly absorbed by it. The initial pulse has a finite support on the outgoing initial ray $u = u_0$, it starts at $v = v_1$ and ends at $v = v_2$. Correspondingly, at $v < v_1$ the geometry is precisely RN with mass M_0 and charge Q . In the test field case, this situation remains unchanged throughout the simulation. In the self-gravitating case, the metric is no longer RN (and no longer static) at $v > v_1$. In particular the mass function (defined below) steadily grows with v .

⁶For similar reasons of numerical-scheme uniformity, we also chose to numerically treat the test scalar field as a self-gravitating one but with an “effectively infinitesimal” pre-factor, which we took here to be $A_0 = 10^{-20}$. (The self-gravity effects are then all multiplied by 10^{-40} , which is smaller than our numerical resolution by many orders of magnitude.)

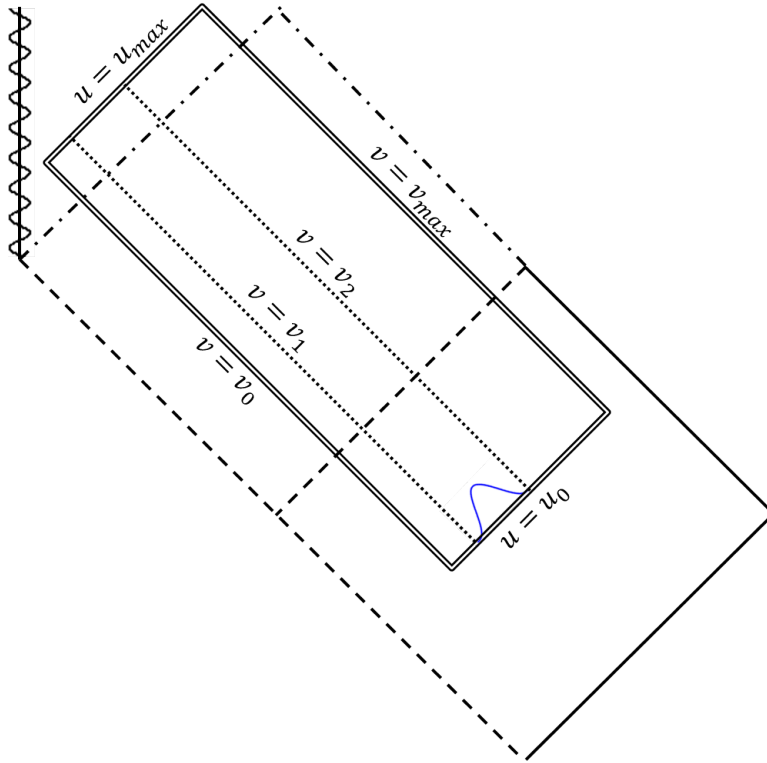


Figure 2: This figure describes the location of the numerical domain of integration with respect to the (initial) RN spacetime. Double lines represent the boundary of numerical domain ($u = u_0$, $u = u_{max}$, $v = v_0$ and $v = v_{max}$); Solid lines represent future and past null infinity ($r = \infty$). Dashed and dashed-dotted lines represent the event horizon ($r = r_+$) and inner horizon ($r = r_-$) respectively. The ingoing scalar field pulse is drawn schematically on the outgoing initial ray $u = u_0$. The pulse is confined (on $u = u_0$) to the range $v_1 \leq v \leq v_2$. The null rays $v = v_1$ and $v = v_2$ (the putative pulse boundaries) are marked by dotted lines.

Two remarks should be made here: First, in Fig. 2 we placed the rectangular numerical domain of integration on the eternal RN background, just for simplicity. However, we can equally well place this rectangle in the RN exterior of a collapsing charged shell, shown in Fig. 1b. In fact, this latter setting is the more physically motivated one, because the physical situation mostly relevant to shock formation is that of charged (or spinning) BH produced in gravitational collapse. The same remark also applies to the self-gravitating set-up illustrated in Fig. 6. Second, ideally we would like to explore the evolution of perturbations up to the CH, located at $v \rightarrow \infty$. For obvious practical reasons we have to pick a finite v_{max} value in our numerics. Nevertheless, below we shall choose a sufficiently large v_{max} , such that the domain of integration will extend deeply into the late-time domain, and will expose the evolution of the various perturbation fields up to the neighborhood of the CH.

The derivation of the model's field equations is fairly standard, it is described in some detail in our preceding paper [16] (see in particular Sec. 2), as well as in other [13] previous works. Overall, we have a system of three evolution equations

$$\Phi_{,uv} = -\frac{1}{r}(r_{,u}\Phi_{,v} + r_{,v}\Phi_{,u}), \quad (2)$$

$$r_{,uv} = -\frac{r_{,u} r_{,v}}{r} - \frac{e^\sigma}{4r} \left(1 - \frac{Q^2}{r^2}\right), \quad (3)$$

$$\sigma_{,uv} = \frac{2r_{,u} r_{,v}}{r^2} + \frac{e^\sigma}{2r^2} \left(1 - \frac{2Q^2}{r^2}\right) - 2\Phi_{,u} \Phi_{,v}, \quad (4)$$

and two constraint equations

$$r_{,uu} - r_{,u} \sigma_{,u} + r(\Phi_{,u})^2 = 0, \quad (5)$$

$$r_{,vv} - r_{,v} \sigma_{,v} + r(\Phi_{,v})^2 = 0. \quad (6)$$

The constraint equations need only be imposed at the initial hypersurface, due to the consistency of the evolution and constraint equations.

We shall occasionally use the *mass function* $m(u, v)$, introduced in Ref. [7], which translates in our coordinates to

$$m = (1 + 4e^{-\sigma} r_{,u} r_{,v})r/2 + Q^2/2r. \quad (7)$$

The location of the event horizon is important in various aspects of this investigation. Here we define it to be the (first) u value where $r_{,v}$, evaluated at the final ingoing ray of the numerical grid $v = v_{max}$, changes its sign from positive to negative. We denote it as u_h . We define the black-hole “final mass” m_{final} as the value of the mass function at the intersection point (u_h, v_{max}) .⁷ In the test field case, $m_{final} = M_0$ of course.

The characteristic initial hypersurface consists of the two null rays $u = u_0$ and $v = v_0$ (below we set $u_0 = v_0 = 0$ in the numerics). On each initial ray we choose initial conditions for two functions, Φ and σ . The remaining function r is dictated [apart from initial conditions at the vertex (u_0, v_0)] by the relevant constraint equation — Eq. (5) at $v = v_0$ and Eq. (6) at $u = u_0$. The choice of initial conditions for σ amounts to a gauge choice: under the gauge transformation $v \rightarrow v'(v), u \rightarrow u'(u)$, the variables r and Φ are unchanged, while σ changes according to

$$\sigma \rightarrow \sigma' = \sigma - \ln\left(\frac{du'}{du}\right) - \ln\left(\frac{dv'}{dv}\right). \quad (8)$$

The gauge is thus determined by the choice of initial conditions for σ along $u = u_0$ and $v = v_0$.

3 BASIC NUMERICAL ALGORITHM

We discretize the field equations on a double-null grid with fixed spacing $\Delta u, \Delta v$. Usually we take $\Delta u = \Delta v = \frac{M_0}{N}$, where M_0 is the initial BH mass and N takes several values in each run (typically 80, 160, 320, 640), in order to verify numerical convergence. The numerical solution progresses along rays of constant u , starting from the initial ray $u = u_0$ and up to the final ray $u = u_{max}$; along each outgoing ray the solution is advanced step by step from $v = v_0$ to $v = v_{max}$. We discretize the evolution equations (2-4) and apply a predictor-corrector scheme, with second order accuracy, as described in Ref. [16].

⁷Note that, owing to the finiteness of v_{max} , the true horizon location is slightly earlier than u_h . Also, the final BH mass is slightly larger than our m_{final} . Both effects are caused by scalar-field inward back-scattering that takes place at $v > v_{max}$. These two deviations are negligibly small, however, owing to asymptotic flatness combined with the large values of v_{max} (always taken to be $\gg m_{final}$) in our simulations. See also footnote 16.

This basic scheme works very well (second order convergence in all unknowns) as long as the domain of integration does not penetrate into the BH. Even if it does penetrate, it still works well as long as Δv_e , the grid size (in outgoing direction) in terms of advanced Eddington coordinate v_e (defined below), is not too large. However, when the horizon is included and $\Delta v_e \gg M_0$, the numerical error typically grows as $e^{\kappa_+ v_e}$ along the EH, where κ_+ is the latter’s surface gravity. If Δv_e is greater than, say, 20 or 25 times M_0 (the actual number depends on κ_+ and on a few other numerical parameters), the truncation error runs out of control and the numerics breaks down. This phenomenon was demonstrated and thoroughly analyzed in Ref. [16].

3.1 The maximal- σ gauge

In order to circumvent this problem of exponentially-growing truncation error, we use the *maximal- σ gauge* (see Sec. 7 in [16]) throughout most of the domain of integration. This gauge is defined by

$$\sigma_{max}(u) = 0, \quad \sigma_v(v) = 0, \quad (9)$$

where $\sigma_v(v) \equiv \sigma(u_0, v)$, namely the initial value of σ along the outgoing characteristic ray; and $\sigma_{max}(u)$ is defined as the maximal value of σ (in the range $v_0 \leq v \leq v_{max}$) along each ray of constant u .⁸ This entirely resolves the aforementioned numerical problem at the event-horizon (as well as an analogous problem which may arise at the inner horizon), as demonstrated in Ref. [16].

3.2 The “singularity approach” gauge variant

At late u values, somewhere beyond the EH, we switch to a new gauge condition (for u), for a reason which we now explain:

As was mentioned in the Introduction, in the presence of self-gravitating scalar field the energy flux across the CH causes the latter to contract: r steadily decreases from r_- down to full contraction at $r = 0$, where the shrinking CH intersects the $r = 0$ spacelike singularity (see Fig. 6). One of the interesting issues which has not been addressed yet is the asymptotic behavior of the shrinking CH (and its neighborhood) on approaching the point of full contraction. This topic is in principle amenable to numerical investigation, provided that the numerical code would be capable of effectively resolving the shrinking CH close to full contraction.

A straightforward approach for improving numerical resolution near full contraction would be to refine the steps in u while r shrinks along the CH. Our basic strategy, however, is to achieve such an effective refinement by controlling the gauge condition for u — as we did earlier for successfully crossing the EH and IH. To this end, we developed a special variant of u -gauge, the *singularity-approach gauge*. This gauge coincides with the maximal- σ gauge up to a certain u value inside the BH, which we denote u_s . Beyond $u = u_s$ we further decrease σ (which effectively amounts to refinement of the u coordinate), by an amount that depends on the smallness of r at the CH. We find that a useful choice for the new σ is via $e^{\sigma_{max}(u)} \propto r(u, v_{max})^2$. (We point out that in our numerical

⁸The gauge condition $\sigma_{max}(u) = 0$ translates into a choice of concrete initial value $\sigma(u, v_0)$ through an extrapolation procedure explained in subsections 7.1 of [16]. The same type of interpolation procedure also applies to the “singularity approach” variant described below.

simulations v_{max} is sufficiently large, such that it effectively represents the CH itself.) The gauge condition at $u > u_s$ is thus

$$\sigma_{max}(u) = 2 \ln [r(u, v_{max})/M_0] + const, \quad \sigma_v(v) = 0. \quad (10)$$

The *const* is fixed by requiring continuity of σ_{max} at $u = u_s$, namely $-2 \ln [r(u_s, v_{max})/M_0]$.

We point out that for the main objective of this paper — exploring the shock structure along the outgoing IH — the fine resolution of the CH close to full contraction is not needed. We could actually use the original maximal- σ gauge (9) throughout the domain of integration. However, we designed our numerical code as a multi-purpose tool, and for this reason we chose to implement the singularity-approach gauge variant in the code.

3.3 Presentation of numerical results

As was mentioned above, in our numerical simulations we used several grid refinement levels, $N = 80, 160, 320, 640$, to test convergent rate and final accuracy. Throughout the paper, in all figures which display data along individual timelike geodesics, we plot the data for both $N = 640$ (solid curves) and $N = 320$ (dashed curves). In all figures but one, there is an excellent agreement between these two resolutions and the two curves effectively overlap, hence the dashed curves cannot be noticed. The only exception is the highly zoomed figure 11, where the dashed lines can barely be noticed (but still, the deviations are small). In figures which display processed timelike geodesics data (such as 5, 9 or 13) or data along null geodesics (figures 14 and 15), we plot the data from the best resolution ($N = 640$) only.

Note also that in all graphs below, we use units in which the initial RN mass parameter is $M_0 = 1$ (in addition to $c = G = 1$), and we also set $u_0 = v_0 = 0$.

4 TEST SCALAR FIELD

In this section we consider the evolution of a test scalar field on a prescribed RN background, and numerically explore the evolving shock-wave in this field. For convenience we denote this test field by ϕ , to distinguish it from its self-gravitating counterpart Φ . This field satisfies the same field equation as Φ , namely $\square\phi = 0$ [and hence same equation as (2)]. However, it has no contribution to the Einstein equations, hence the geometry remains RN throughout.

We first describe the set-up of initial data for ϕ . Then we introduce a family of timelike infalling geodesics, which probe ϕ inside the BH as a function of their proper time τ and thereby expose the effective shock-wave structure. Then we move on to analyze the shock properties, and in particular how its width decreases with infall time.

4.1 Basic parameters and initial conditions

The test scalar field propagates in the RN geometry, which in Schwarzschild coordinates reads

$$ds^2 = -f(r)dt^2 + f(r)^{-1}dr^2 + r^2d\Omega^2, \quad (11)$$

where $f \equiv 1 - 2M/r + Q^2/r^2$. The EH and IH are located at

$$r_{\pm} = M \pm \sqrt{M^2 - Q^2}. \quad (12)$$

The surface gravity at the IH and EH is given by

$$\kappa_{\pm} = \frac{\sqrt{M^2 - Q^2}}{r_{\pm}^2}.$$

We choose here mass parameter $M = 1$ ⁹ (which actually reflects our choice of units), and charge $Q = 0.92$.¹⁰ The event and inner horizon values are then $r_+ \simeq 1.392$ and $r_- \simeq 0.608$ respectively, and the corresponding IH surface gravity is $\kappa_- \simeq 1.06$.

The location of the numerical grid with respect to the RN background is illustrated in Fig. 2. While the outgoing initial ray $u = u_0$ is located outside the EH, the ingoing ray $v = v_0$ penetrates into the BH and subsequently crosses the IH as well. In practice we set the values of the two initial null rays to be $u_0 = v_0 = 0$ for convenience.

The initial value for the metric variable σ was chosen so as to conform with the “singularity approach” gauge condition described in Sec. 3.2. In particular, σ vanishes along the $u = u_0$ initial ray. The initial data for the scalar field are taken to be those of ingoing pulse at $u = u_0$, as schematically shown in Fig. 2 (in particular ϕ vanishes along $v = v_0$). The ingoing pulse on $u = u_0$ has a finite support at $v_1 \leq v \leq v_2$, and we choose it such that both ϕ and its derivative are smooth at the edges $v_{1,2}$. Specifically we take the symmetric initial pulse

$$\phi(u_0, v) = \phi_0(v) \equiv \begin{cases} \frac{64(v-v_1)^3(v_2-v)^3}{(v_2-v_1)^6} & | \ v_1 \leq v \leq v_2 \\ 0 & | \ otherwise \end{cases} \quad (13)$$

The polynomial form was selected due to its simplicity. The pre-factor 64 was introduced such that the ingoing pulse has a unit amplitude.¹¹ In our test-field runs we chose $v_1 = 1$, $v_2 = 3$. Overall the domain of integration was taken to be $u_0 = v_0 = 0$, $u_{max} = 105$, and $v_{max} = 120$. The value of r at the initial vertex was $r(u_0, v_0) = 5$, and along the outgoing initial ray it grew monotonically up to $r(u_0, v_{max}) \simeq 52.8$.

The numerical code was then run with the four resolutions $N = 80, 160, 320, 640$, in order to control accuracy and convergence rate, as described in Sec. 3.

⁹As was already mentioned in Sec. 2, our code actually solves the electrovac Einstein equations and numerically construct the RN metric (in the chosen gauge). Consequently there is a small numerical drift in M . This drift, however, is of order $\sim 2 \cdot 10^{-7}$ and does not affect any of our results.

¹⁰This value of Q was chosen to obtain κ_- value close to 1.

¹¹As was already noted in footnote 6, in the numerical run we actually multiply this initial function by an extremely small overall factor $A_0 = 10^{-20}$ (so as to numerically “mimic” a test field). Throughout this section all the results for ϕ are presented with this artificial pre-factor scaled-out (namely, we divide the actual numerical data by A_0).

4.1.1 Double-null Eddington coordinates

We denote the Double-null Eddington coordinates by u_e and v_e . In the RN background (outside the BH) they are defined by

$$v_e \equiv t + r_*, \quad u_e \equiv t - r_*,$$

where r_* is the tortoise coordinate given by

$$r_*(r) = r + \frac{r_+^2}{r_+ - r_-} \ln |r - r_+| - \frac{r_-^2}{r_+ - r_-} \ln |r - r_-| + \text{const}. \quad (14)$$

The integration constant in this equation may be chosen at will. Owing to time-translation symmetry these coordinates are defined up to a global displacement. We find it convenient to set $u_e = 0$ at the initial ray $u = u_0$, and to set $v_e = 0$ at the end of the injected pulse, namely at $v = v_2$. This choice fixes the integration constant in Eq. (14), by requiring $r_* = 0$ at $r(u_0, v_2)$.

We shall hereafter reserve the symbols u, v to the double-null coordinates that we actually use in the numerical simulation (namely, those defined by the gauge conditions prescribed in Sec. 3.2). Later we shall need to use the relation $v_e(v)$. This function is easily determined numerically, at the outgoing initial ray $u = u_0$, using $v_e - u_e = 2r_*$. Since u_e vanishes at that ray by definition, we obtain

$$v_e(v) = 2r_*(r(u_0, v)). \quad (15)$$

4.2 Family of timelike geodesics

Following Ref. [22], we consider here a family of timelike geodesics related to each other by time translation, and use them to probe the BH interior. We shall refer to such a family as a *time-translated set of geodesics* (TTSG). In the present case of test perturbation, this family consists of exact RN geodesics, all sharing the same energy ($E = -u_t$) and angular momentum ($L = u_\varphi$) values, which fall into the BH. Each geodesic is marked by a typical timing parameter. We adopt here the same timing parameter as in [22], namely v_{eh} — the value of Eddington null coordinate v_e at the moment of EH crossing.

For concreteness and simplicity, we choose here the set of geodesics $E = 1, L = 0$, representing a family of infalling observers on marginally-bound radial geodesics. These observers will probe the scalar field inside the BH as a function of their proper time τ and infall time parameter v_{eh} . We set the proper time value $\tau = 0$, at each geodesic, at the moment of EH crossing. The parameter v_{eh} for each geodesic is determined from the value of v at horizon crossing, via Eq. (15).

Our numerical code produces values of the unknowns r, σ, Φ on a discrete set of grid points in the (u, v) coordinates, as described in Sec. 3. However, for the shock-wave analysis we shall have to evaluate these functions on the aforementioned radial timelike geodesics. The latter may be considered as a set of bent curves $v(u)$, obtained from the geodesic equation (see Appendix A.1 for more details). Generically, these curves do not pass at grid points. Therefore, at each grid value of u we interpolate our numerical results (given on the discrete v values) to the desired value $v(u)$ on the geodesic. To this end we use second-order interpolation.

4.3 Shock wave in the scalar field

The effective shock-wave formation in the test scalar field ϕ is demonstrated in Fig. 3, which displays $\phi(\tau)$ for various infalling geodesics, labeled by their v_{eh} values. In these geodesics, whereas r monotonically decreases towards r_- , the scalar field ϕ is non-monotonic: it decreases at some stage but then increases again (this is better seen in panel b, in which τ is shifted to enable visual separation of the different geodesics). The evolving shock structure manifests itself as a rapid sharpening (with increasing v_{eh}) of both the decrease phase and the subsequent increase phase. The increase phases in all geodesics (except the earliest ones, say $v_{eh} = 4 - 5$) form an effectively vertical line. These vertical lines, in all geodesics, occur approximately at the same proper time ($\tau \simeq 0.7438$), hence they all overlap in panel a, forming the “wall like” structure. Also, these vertical sections occur in all geodesics at approximately the same r value, namely $r = r_-$.¹²

In order to enable visual separation of the different geodesics, such that the shock (and pre-shock) phase of the individual geodesics would be seen, in panel b the τ value of each geodesic is shifted by a certain amount, proportional to its v_{eh} .

Whereas Fig. 3 demonstrated the shock formation phase by presenting relatively early geodesics ($v_{eh} \leq 15$), Fig. 4a displays much later infalling geodesics $20 \leq v_{eh} \leq 100$. The shock structure is now fully developed: It takes the form of a vertical line, located at the same proper time for all geodesics. It is placed just at the τ value that corresponds to $r = r_-$ (the dashed vertical line).

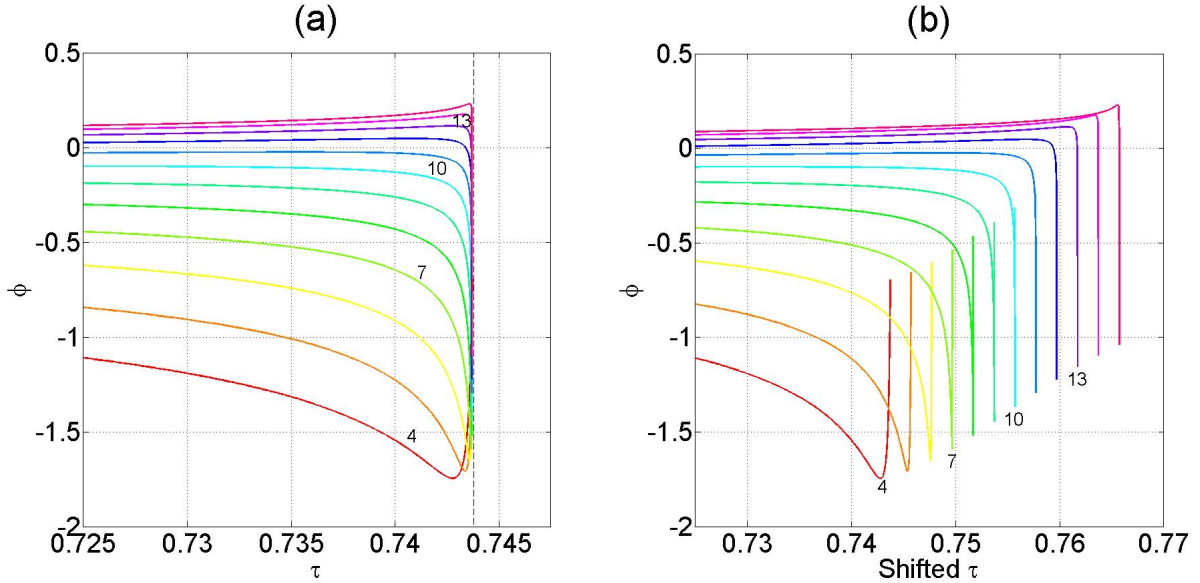


Figure 3: Shock-wave formation in the test scalar field ϕ . Both panels present ϕ as a function of proper time τ along a family of radial timelike geodesics with $E = 1$. Panel a uses true τ values at each geodesic (with $\tau = 0$ set at EH crossing); panel b uses τ values artificially shifted by an amount $(i - 1) \times 2 \cdot 10^{-3}$ for the i -th geodesic ($i = 1, \dots, 12$, corresponding to $v_{eh} = 4, \dots, 15$), in order to enable clear visual separation of the different geodesics. Geodesics are distinguished by different colors and different v_{eh} values. v_{eh} increases by increments of 1 from the bottom/left ($v_{eh} = 4$) to the top/right ($v_{eh} = 15$). The vertical dashed line in panel a represents the RN theoretical τ value of IH crossing, $\tau \simeq 0.7438$.

¹²Note that in the way we set the family of geodesics, they all share the same function $r(\tau)$, due to time-translation invariance.

4.3.1 Shock resolution and shock Sharpening

Figures 3a and 4a made it clear that the shock structure involves extremely short τ intervals — which further shorten with increasing v_{eh} . Still, we can resolve the shock by using a logarithmic scale for τ . To this end, however, we shall have to use the shifted variable $|\tau - \tau_{final}|$, where τ_{final} is the last proper time value for each geodesic (achieved at $u = u_{max}$ arrival). Figure 4b provides such a logarithmic representation of ϕ as a function of $|\tau - \tau_{final}|$, for the same set of geodesics as in Fig. 4a (namely, $20 \leq v_{eh} \leq 100$).

This figure demonstrates that the shock structure [which actually enfolds alternating domains of decreasing and increasing $\phi(\tau)$] is essentially unchanged while v_{eh} increases. The main effect of the increase in v_{eh} is to shorten the proper-time width of the configuration. This sharpening is expressed in Fig. 4b by the overall rightward shift in the logarithmic scale, with increasing v_{eh} .

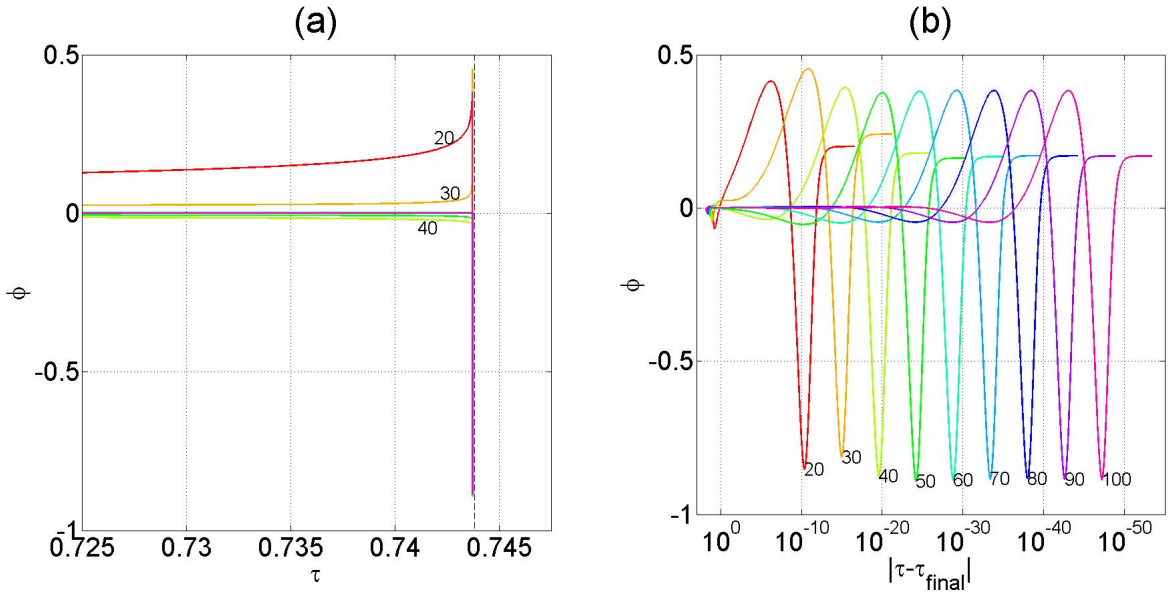


Figure 4: Shock-wave structure at late time. The graph displays $\phi(\tau)$ along a family of radial timelike geodesics with $E = 1$, this time for later geodesics, $20 \leq v_{eh} \leq 100$. The different geodesics are again marked by different colors and different v_{eh} values; v_{eh} increases by increments of 10 from top/left ($v_{eh} = 20$) to bottom/right ($v_{eh} = 100$). Panel a uses a linear scale in τ , clearly showing the well-developed shock structure (the vertical line at the right); panel b uses a logarithmic scale in $|\tau - \tau_{final}|$, where τ_{final} is the final τ value at $u = u_{max}$. The vertical dashed line in panel a again represents the theoretical τ value of IH crossing in RN, $\tau \simeq 0.7438$. Panel b exhibits the sharpening of the shock — the width of the scalar field pulse exponentially decreases with v_{eh} , as inferred from the apparently “rigid” shift to the right (with respect to the logarithmic scale) with increasing v_{eh} .

According to the analysis of Ref. [22], the decrease in any proper-time width scale $\Delta\tau$ associated with the scalar-field shock-like signal should be exponential (for sufficiently late geodesics): $\Delta\tau \propto e^{-\kappa v_{eh}}$, where $\kappa \equiv \kappa_-$ is the surface gravity at the inner horizon. To test this prediction we chose here a specific width scale $\Delta\tau$: the difference in τ between the minimum and maximum points in

$\phi(\tau)$ ¹³ at each geodesic. The results are presented in Fig. 5. As expected $\Delta\tau$ decays exponentially, in nice agreement with the theoretically predicted rate $e^{-\kappa v_{eh}}$ ¹⁴.

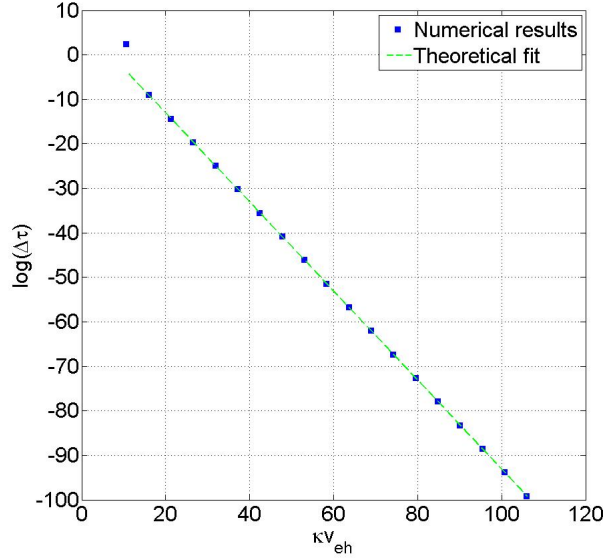


Figure 5: Exponential sharpening rate of the test scalar field shock, as demonstrated by the decrease of $\Delta\tau$ with increasing v_{eh} . Each point represents a single $E = 1$ radial timelike geodesic; the geodesics are in the range $10 \leq v_{eh} \leq 100$, with increments of 5. The straight diagonal dashed green line is the theoretical fit, $\ln(\Delta\tau) = -\kappa v_{eh} + \text{const}$. All geodesics show excellent agreement with the theoretical fit, except the first geodesic $v_{eh} = 10$ (which is seemingly too early for the late-time theoretical relation to hold).

Note that Marolf and Ori mainly focused in their shock-wave analysis [22] on the late time domain, where the background geometry is approximately static. However, as Fig. 3 demonstrates, the shock-like behavior can also be detected for very early infalling geodesics, even for e.g. $v_{eh} = 4$.¹⁵ Notice, in addition, that the nice agreement of the points in Fig. 5 with the straight diagonal dashed line (representing the theoretical sharpening rate $\Delta\tau \propto e^{-\kappa v_{eh}}$) starts already at $v_{eh} \approx 15$.

5 SELF-GRAVITATING SCALAR FIELD PERTURBATION

In the case of self-gravitating scalar perturbation, the shock wave manifests itself in the scalar field Φ and also in the metric. In this section, after describing the set-up of the problem, we shall first

¹³To be more specific, these are the (last) maximum and minimum points in the profile shown in Fig. 4b for each geodesic.

¹⁴Similar results were obtained for another choice of typical width, the *full width at half maximum* of $\phi(\tau)$ at the various geodesics.

¹⁵We point out that the observation of the shock-like behavior is obviously scale dependent: clearly, a sufficient zoom on the τ scale in e.g. Fig. 3 would resolve the sharp features. We argue, however, that since the τ scale in Fig. 3 is already rather small (the overall horizontal scale of panel a is ≈ 0.025 , which is $\ll 1$), the sharp features seen in that panel indeed indicate a shock-like behavior.

present the shock in Φ , and subsequently the shock in the metric function r . Then we shall re-analyze the shock in r using a family of ingoing null geodesics (rather than timelike ones).

5.1 Set-up and initial conditions

The setup in the present case is similar to the test-field case presented in Sec. 4, except that our scalar field is now self-gravitating. Initially (at $v < v_1$) we have an exact RN geometry with mass $M_0 = 1$ and charge $Q = 0.95$. Then at $v_1 < v < v_2$ we inject the ingoing scalar-field pulse, as schematically shown in Fig. 6. (Note that Φ vanishes at the ingoing initial ray $v = v_0$.) The scalar field then spreads throughout the domain $v > v_1$. At later times the field back-scatters and decays, and eventually we have an approximate RN geometry at large v , with the same charge $Q = 0.95$ but with final mass $m_{final} > M_0$.

The injected scalar field pulse is taken to be of the form

$$\Phi(u_0, v) = A \phi_0(v),$$

where $\phi_0(v)$ is the basic finite-support pulse function given in Eq. (13), and A is a free amplitude parameter. We chose here the values $A = 0.115$ along with pulse boundary parameters $v_1 = 1$, $v_2 = 7$. With this choice the final mass becomes $m_{final} \cong 1.4587$.¹⁶ The corresponding inner-horizon surface gravity parameter is $\kappa \simeq 8.94$. We picked these parameters (despite the relatively large resultant value of κ) in order to achieve significant focusing of the CH within the numerical domain.¹⁷

The initial conditions for the metric function σ are set in accord with the “singularity approach” gauge condition presented in Sec. 3.2. In particular, σ vanishes along the $u = u_0$ initial ray. The initial data for r are calculated, along both initial rays, from the constraint equations. As before, we set $u_0 = v_0 = 0$ for convenience. The other boundaries of the domain of integration are $u_{max} = 182$ and $v_{max} = 120$. The value of r at the initial vertex is again $r(u_0, v_0) = 5$, and along the outgoing initial ray it grows monotonically up to $r(u_0, v_{max}) \simeq 44.0$.

Note that there are two different RN phases in spacetime: (i) an *exact* initial RN geometry at $v < v_1$, and (ii) an *approximate* RN geometry at late time, namely $v \gg 1$.¹⁸ The effective shock wave is essentially a phenomenon that takes place at late times, hence it is the approximate RN domain (ii) that will be mostly relevant to the shock analysis below. The event and inner horizon values of this domain are $r_+ \simeq 2.566$ and $r_- \simeq 0.352$ respectively.

¹⁶In principle m_{final} should be defined as the limit of the mass function m along the EH as $v \rightarrow \infty$. In practice we only monitor the evolution up to v_{max} , hence we take m_{final} to be the mass function evaluated at the EH at $v = v_{max}$. We verified, by inspecting the large- v freezing of $m(v)$ along the horizon, that the change in this function at $v > v_{max}$ is negligible, probably smaller than 10^{-6} .

¹⁷The focusing effect, in this context, is a gradual decrease of r along the CH. While we do not actually reach the CH in our numerical simulation (it corresponds to $v \rightarrow \infty$), we get relatively “close” to it in terms of the behavior of the various fields, and in particular Φ and r . With the choice $A = 0.115$ we get a significant focusing in our numerical domain: r shrinks along $v = v_{max}$ down to $\approx 10^{-2}$ or even less. This significant focusing is advantageous as it allows a better visibility of the shock behavior in r (discussed in Sec. 5.3).

¹⁸A more precise condition would be $v - v_2 \gg m_{final}$ (but in the present case the two conditions are essentially the same).

possible the behavior of radial TTSG in exact RN. In the latter case we have

$$\dot{r} = -\sqrt{E^2 - \left(1 - \frac{2M}{r} + \frac{Q^2}{r^2}\right)},$$

which for $E = 1$ reduces to $-(2M/r - Q^2/r^2)^{1/2}$. In the self-gravitating case, we replace the constant M by the mass function m . Correspondingly we set the initial condition for the geodesics at $u = u_0$ to be

$$\dot{r}(u_0, v) = -\sqrt{\frac{2m(u_0, v)}{r(u_0, v)} - \frac{Q^2}{r(u_0, v)^2}}. \quad (16)$$

At the large- v limit this one-parameter set of geodesics indeed approaches the $E = 1$ radial TTSG in RN, as desired.

Here again, for all infalling geodesics we set $\tau = 0$ at EH crossing, as we did in the test-field case.

5.1.2 Outgoing Eddington-like coordinate v_e

In the test-field case we have used the Eddington coordinate v_e (evaluated at EH crossing) to parametrize the infalling geodesics. However, in the self-gravitating case the double-null Eddington coordinates are not uniquely defined, as the metric is no longer static. We therefore introduce here the extended notion of *Eddington-like* outgoing null coordinate, and denote it as before by v_e . The function $v_e(v)$ is hereby *defined* by Eq. (15), similar to the test-field case.¹⁹ As before we set $u_e = 0$ at $u = u_0$ and $v_e = 0$ at $v = v_2$ (end of pulse injection), which in turn fixes the integration constant in Eq. (14) by dictating $r_* = 0$ at $r(u_0, v_2)$.

Once the Eddington-like null coordinate v_e is defined, the infalling timelike geodesics are parametrized by their v_{eh} , namely the value of v_e at EH crossing.

Note that in the present case v_e vanishes at $v = v_2 = 7$, whereas the domain of integration starts at $v = v_0 = 0$. The range $0 < v < 7$ thus corresponds to negative v_e . Accordingly, some of the infalling geodesics admit *negative* v_{eh} values, as can be seen in e.g. Fig. 7. (But this negative value of v_e or v_{eh} has no special significance.)

5.2 Shock wave in the scalar field

The shock wave in the scalar field is demonstrated in Figs. 7 and 8, by displaying $\Phi(\tau)$ for various infalling geodesics. The early phase of shock formation is presented in Fig. 7: Whereas early geodesics with say $v_{eh} < -2$ look smooth, geodesics with larger v_{eh} exhibit a sharp feature. In fact, this sharp feature involves a rapid decrease followed by an even more rapid increase: This can be seen in e.g. the geodesic $v_{eh} = -1.8$. The same behavior also occurs in later geodesics (-1.6 to -1), although in these geodesics the decrease-increase phases are too narrow and cannot be distinguished without additional zoom.

¹⁹The function $r_*(r)$ appearing in this formula is given in Eq. (14). It involves the parameters r_+ and r_- , which in the RN case are given by $M \pm (M^2 - Q^2)^{1/2}$. In the self-gravitating case, for the sake of defining v_e we replace M by $m(u_0, v_{max}) \cong 1.4591$ (which is very close to m_{final}).

Figure 8 shows much later geodesics, with $20 \leq v_{eh} \leq 70$. In the linear scale of panel a, all the geodesics form a seemingly vertical “wall”, at $\tau \approx 1.789$. This value agrees, to a very good approximation, with the proper-time interval $\tau_{RN} \cong 1.7889$ to move from the EH to the IH, for an $E = 1$ radial geodesic in an RN geometry with $Q = 0.95$ and mass $m_{final} \cong 1.4587$. This proper-time value τ_{RN} is marked in Fig. 8a by a vertical dashed line.

Note that in the early phase shown in Fig. 7, unlike its test-field counterpart in Fig. 3a, the different geodesics develop their shocks at notably different τ values. This directly results from the dynamical character of the nonlinearly-perturbed spacetime, which breaks time-translation invariance. On the other hand, in the late-time phase (Fig. 8a) the spacetime is approximately static, hence the shocks of all geodesics fall approximately at the same τ value, ≈ 1.789 .

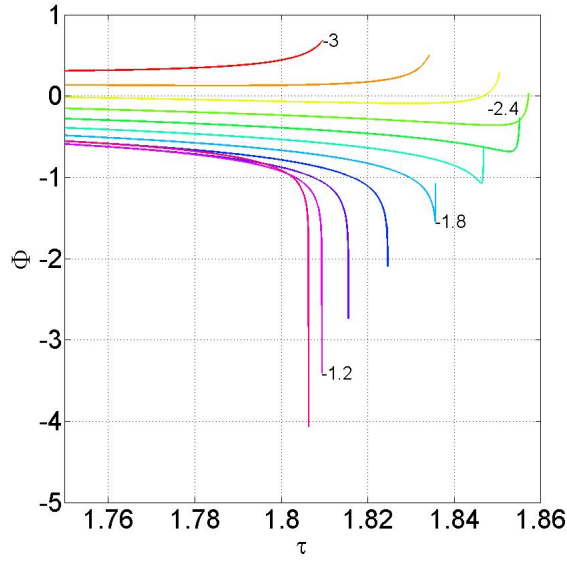


Figure 7: Numerical results for the self-gravitating scalar field Φ as a function of proper time τ along the family of radial timelike geodesics described in the main text. The geodesics are distinguished by different colors and different values of v_{eh} (the geodesic’s v_e value at EH crossing); v_{eh} increases by increments of 0.2 from the top of the graph ($v_{eh} = -3$) to the bottom ($v_{eh} = -1$). We set $\tau = 0$ at the EH crossing event for each geodesic. The shock formation process manifests itself as a gradual sharpening of the scalar field profile with increasing v_{eh} . The smaller value of the increments (compared to the test-field case shown in Fig. 3), and the negative values of v_{eh} in the present case, imply a more rapid shock formation process in the self-gravitating case. This may be explained by the higher κ value in the present case (8.94 compared to 1.06).

5.2.1 Shock resolution and shock sharpening

To resolve the shock structure, in Fig. 8b we use a logarithmic horizontal scale. To this end we again employ the shifted variable $|\tau - \tau_{final}|$, where, recall, τ_{final} is the last proper time value for each geodesic (at $u = u_{max}$ arrival). This panel shows that in the self-gravitating case too, for sufficiently late geodesics the shock shape is essentially unchanged while v_{eh} increases — apart from a uniform rightward motion, which expresses an overall shrinking of the shock’s τ scale.

To quantify the rate of shock sharpening, we again resort to the width parameter $\Delta\tau$, defined to be the difference in τ between the minimum and maximum points in $\Phi(\tau)$ (those seen in Fig. 8b) at each geodesic. Figure 9 displays $\Delta\tau$ of the various geodesics as a function of their infall time v_{eh} . It again shows excellent agreement with the exponential sharpening rate $\Delta\tau \propto e^{-\kappa v_{eh}}$ (represented by the straight diagonal dashed line), theoretically predicted in Ref. [22] (for late-infall geodesics). Exceptional are the two earliest geodesics shown in the graph, namely $v_{eh} = 0$ and $v_{eh} = 5$.

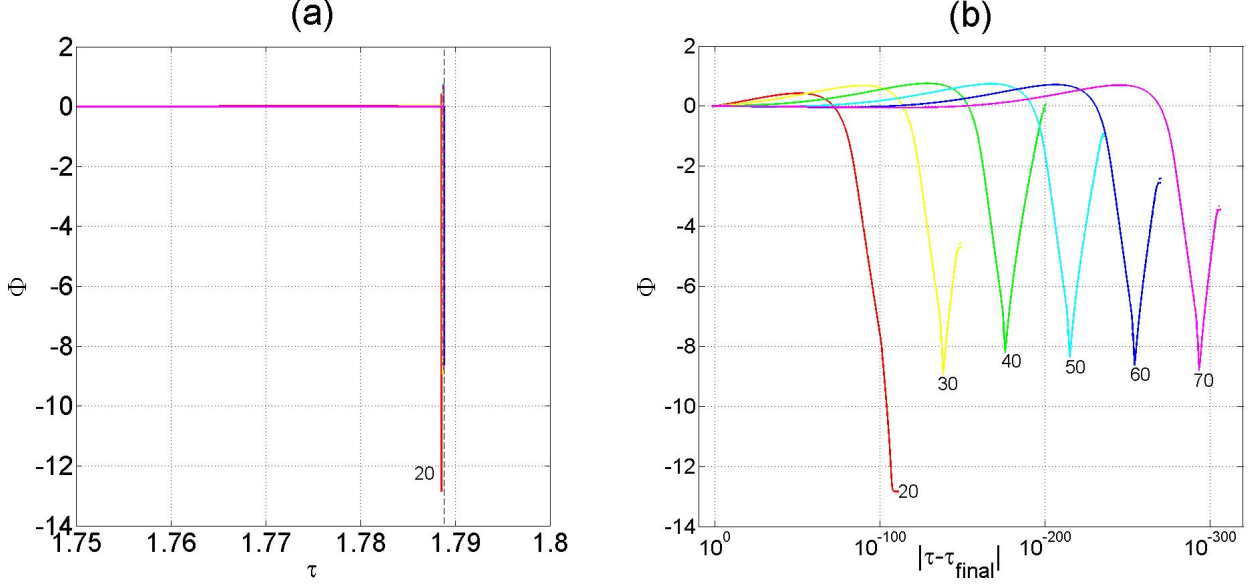


Figure 8: Numerical results for Φ as a function of proper time τ along a family of radial timelike geodesics. Panel a employs a linear scale in τ ; panel b employs a logarithmic scale in $|\tau - \tau_{final}|$, to allow shock resolution. Both panels display the same set of geodesics. The different geodesics are marked by different colors and different v_{eh} values; v_{eh} increases by increments of 10 from bottom/left ($v_{eh} = 20$) to top/right ($v_{eh} = 70$). The vertical dashed line in panel a represents $\tau_{RN} \cong 1.7889$, which is the proper-time moment of IH crossing for a marginally-bound radial geodesic in RN spacetime with $Q = 0.95$ and mass $m_{final} = 1.4587$. Panel b exhibits the sharpening of the shock: The width of the scalar-field profile seems to decrease exponentially with v_{eh} . It may also be seen that the shape of the scalar-field profile at late times (say $v_{eh} \gtrsim 40$) is essentially unchanged.

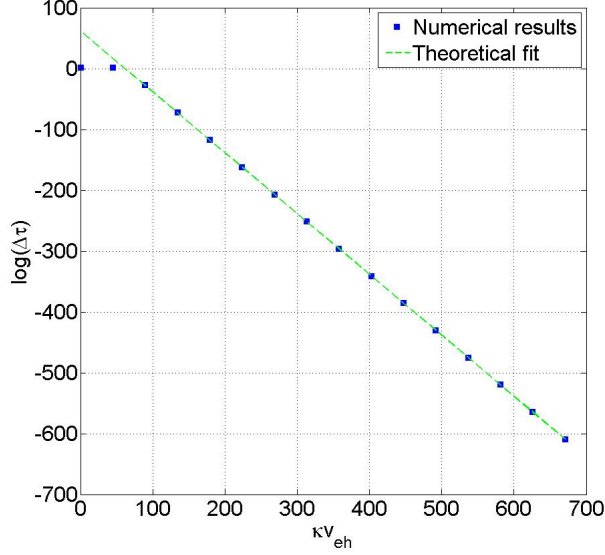


Figure 9: Exponential sharpening rate of the self-gravitating scalar field shock, as demonstrated by the decrease of $\Delta\tau$ with increasing v_{eh} . Each point represents a single timelike radial geodesic; the geodesics are in the range $0 \leq v_{eh} \leq 75$, with increments of 5. The straight dashed green line is the theoretical fit, $\ln(\Delta\tau) = -\kappa v_{eh} + \text{const}$. All geodesics show excellent agreement with the theoretical fit, except the two earliest ones ($v_{eh} = 0, 5$).

5.3 Shock Wave in r

We next consider the shock wave in the variable r , which is in fact a *metric function* (in the sense that $r^2 = g_{\theta\theta}$). We use the same numerical setup and same family of timelike geodesics described in subsection 5.1. Figure 10 displays $r(\tau)$ for various timelike geodesics. The early geodesics shown in panel a reveal the initial phase of shock formation: While the earliest geodesics look fairly smooth, the latest ones develop an approximately-vertical section (clearly seen for e.g. $v_{eh} \geq -1.4$).

Panel b of Fig. 10 presents late geodesics, demonstrating the nature of the fully-developed shock in r . Note that although a single purple/red curve is visible in this graph, it actually enfolds many late geodesics in the range $v_{eh} \geq 10$. The dotted black curve displays $r(\tau)$ for an $E = 1$ radial geodesic in pure RN metric with the final asymptotic mass $m_{final} \cong 1.4587$ (and $Q = 0.95$). The horizontal dashed line marks the corresponding IH value, $r_- \cong 0.35177$, of this asymptotic RN metric. The graph clearly shows that to a very good approximation, all late geodesics follow the pure-RN geodesic curve — but only at $r > r_-$. When r approaches r_- , $r(\tau)$ abruptly decreases, forming the red vertical section. This is the (fully developed) gravitational shock wave.

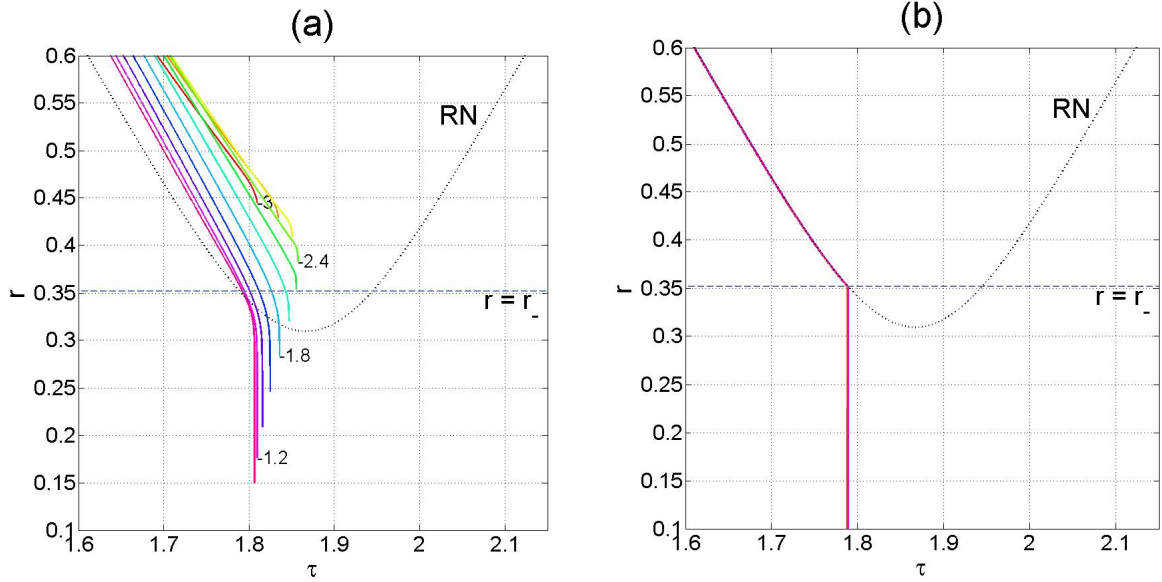


Figure 10: Numerical results for $r(\tau)$ along the prescribed family of radial timelike geodesics. The black dotted curve denoted “RN” is the theoretical $r(\tau)$ function for an $E = 1$ radial geodesic in the asymptotic RN solution (with parameters $m = 1.45867$, $Q = 0.95$); the dashed horizontal line represents the inner-horizon r value ($r_- \cong 0.35177$) in that asymptotic RN. The solid curves represent the numerical results for $r(\tau)$ along the various geodesics. Panel a shows early geodesics (negative v_{eh} regime, from -3 to -1). The different geodesics are marked by different colors and different v_{eh} values; v_{eh} increases by increments of 0.2 . Panel b presents late geodesics (positive v_{eh} in the range $10 \leq v_{eh} \leq 80$, with increments of 5). In this scale these 15 different geodesics are unresolved, they are all represented by the same red/purple curve. (The differences between these geodesics will be shown in the zoomed figure 11.)

Figure 11 zooms on the late geodesics near the “corner” at $r = r_-$. It illustrates how, when v_{eh} increases, (i) the “corner” at each individual geodesic sharpens, and (ii) the function $r(\tau)$ becomes closer (at $r > r_-$) to its asymptotic-RN counterpart. As $v_{eh} \rightarrow \infty$ the limiting function $r(\tau)$ should just coincide with the asymptotic RN curve all the way down to r_- , then it should abruptly fall towards $r = 0$.

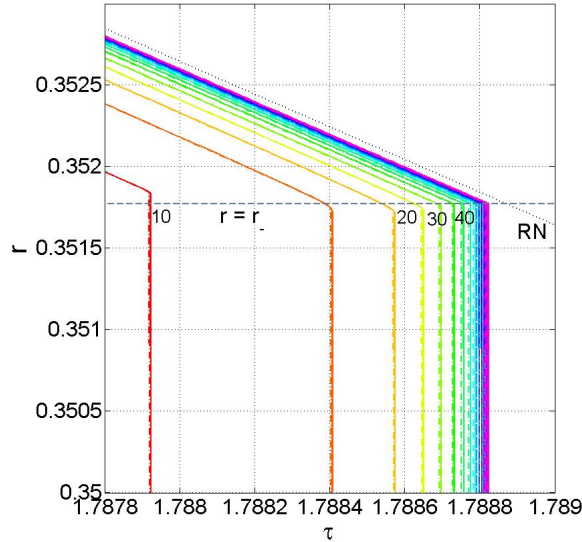


Figure 11: Zoom on panel b of figure 10, near the “corner”. The figure shows $r(\tau)$ for the same set of 15 late geodesics as in Fig. 10b, but this time (most of) the individual geodesics are resolved. The different geodesics are marked by different colors and different v_{eh} values; v_{eh} increases by increments of 5 from left ($v_{eh} = 10$) to right ($v_{eh} = 80$). Recall that each of the timelike geodesics is actually represented (here and throughout the paper) by *two* curves, presenting our two best numerical resolutions $N = 640$ (solid curve) and $N = 320$ (dashed curve). In this highly zoomed figure, these two resolutions can be distinguished, although barely.

5.3.1 Shock resolution and shock sharpening

We again employ a logarithmic presentation (in $\tau - \tau_{final}$) to resolve the exponentially small proper-time duration of the shock. Figure 12 demonstrates that in this case too, for late geodesics the function $r(\tau - \tau_{final})$ just shifts rightward with increasing v_{eh} , with no appreciable change in its form. This shift indicates an exponential decrease in the shock’s proper-time scale.

To quantify this sharpening, we again need to define a measure $\Delta\tau$ of the shock width (for each geodesic). In this case we cannot take it to be the proper-time duration between maximum and minimum points because, unlike the scalar field, $r(\tau)$ is monotonic in the relevant domain. Instead, we can take $\Delta\tau$ to be the proper time it takes for r to change from a certain value to another, smaller one. For concreteness, we define here $\Delta\tau$ to be the proper-time duration to drop from $0.75 r_-$ to $0.25 r_-$ along the geodesic. (Here, as before, $r_- \cong 0.35177$ is the IH radius of the late-time asymptotic RN geometry.) Figure 13 displays this width as a function of v_{eh} , confirming again the exponential sharpening relation $\Delta\tau \propto e^{-\kappa v_{eh}}$ predicted in Ref. [22].

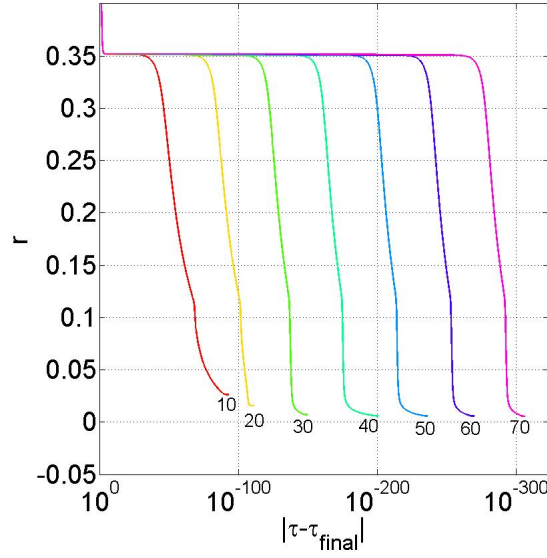


Figure 12: Logarithmic presentation of the numerical results for r as a function of $|\tau - \tau_{final}|$, along the prescribed family of radial timelike geodesics. The different geodesics are marked by different colors and different v_{eh} values; v_{eh} increases by increments of 10 from left ($v_{eh} = 10$) to right ($v_{eh} = 70$).

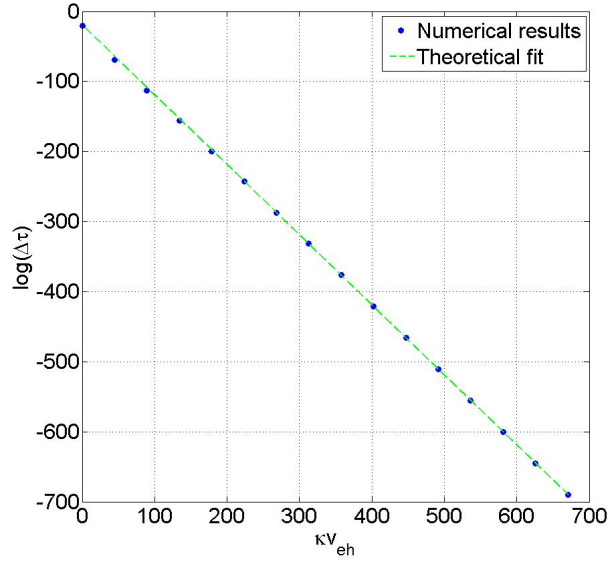


Figure 13: Exponential shock sharpening as demonstrated by the decrease of $\Delta\tau$, the difference between $\tau(r = 0.75 r_-)$ and $\tau(r = 0.25 r_-)$. Each point represents a single timelike radial geodesic; the geodesics are in the range $0 \leq v_{eh} \leq 75$, with increments of 5. The diagonal dashed green line is a fit to the theoretical relation $\ln(\Delta\tau) = -\kappa v_{eh} + const$. The graph indicates a very good agreement between the theoretical prediction and the numerical results, especially for the late-time geodesics (e.g. $v_{eh} \gtrsim 20$).

5.4 Probing the shock with ingoing null geodesics

So far we used timelike geodesics to probe the shock. It is also possible, however, to use *null* geodesics for that purpose. To this end we should focus on the dependence of r (or Φ , or any other variable of interest) on the affine parameter λ along a given null geodesic. The shock will manifest itself as a sharp feature in $r(\lambda)$ [or $\Phi(\lambda)$].

Indeed, timelike geodesics may be considered more “physical” than their null counterparts, as they represent the actual orbits of physical probes. However, null geodesics are more convenient in several respects: First of all, the usage of null rather than timelike geodesics reduces the amount of arbitrariness involved in the construction of the set of ingoing geodesics, because the degree of freedom of choosing E no longer exists. In particular, if we restrict attention to radial geodesics (which is obviously the natural thing to do for spherically-symmetric backgrounds), the family of null geodesics becomes *unique*. Second, there is no need to solve the geodesic equation in the null case, because radial null orbits are trivial. In fact, our numerical results are given on ingoing null geodesics — namely the grid lines $v = \text{const}$ — already in the first place. All that is needed, in order to generate the requested function $r(\lambda)$ [or $\Phi(\lambda)$], is to compute $\lambda(u)$ along the desired $v = \text{const}$ rays. This is an easy task, as we show in Appendix A.2.

Note that along each null geodesic, $\lambda(u)$ is uniquely defined up to two free parameters: A global multiplicative constant, and a global shift. Here we fix both parameters at the EH (for each ingoing geodesic), by setting $\lambda = 0$ and $dr/d\lambda = -1$ at horizon crossing.

In what follows we shall focus on the shock wave in r . The function $r(\lambda)$ along an ingoing null geodesic admits two convenient properties: (i) it decreases monotonically, and (ii) it becomes exactly linear in the pure RN case (see Appendix A.2.1). Due to these properties, a 3-dimensional graphics turns out to be especially useful for presenting the shock in r . Figure 14 demonstrates the shock formation phase by displaying $r(\lambda)$ for early ingoing null geodesics ($-4 < v_e < 6$), as a function of their v_e value. Notice the smoothness of $r(\lambda)$ for very early geodesics (say $v_e \lesssim 1$), and the development of an apparent “corner” (at $r \simeq r_-$) for larger v_e .

Figure 15 does the same, but for much later geodesics (up to $v_e \approx 85$). In addition, it also displays the corresponding function $r(\lambda)$ for radial null geodesics in the exact RN geometry²⁰ (the straight dotted black lines). This function is given by $r(\lambda) = r_+ - \lambda$ (independent of v_e). The 3d graph clearly demonstrates (i) the nice agreement of $r(\lambda)$ with its RN counterpart up to a clear “break line”, which occurs at $r \approx r_- \simeq 0.352$, and (ii) the sharp, seemingly-vertical, decline of $r(\lambda)$ beyond that break line. The vertical “wall” that forms at $r \lesssim r_-$ is perhaps the clearest visual presentation of the shock phenomenon.

²⁰This RN geometry is taken with the appropriate asymptotic parameters, namely $Q = 0.95$ and $M = m_{\text{final}}$, yielding $r_+ \simeq 2.566$ and $r_- \simeq 0.352$.

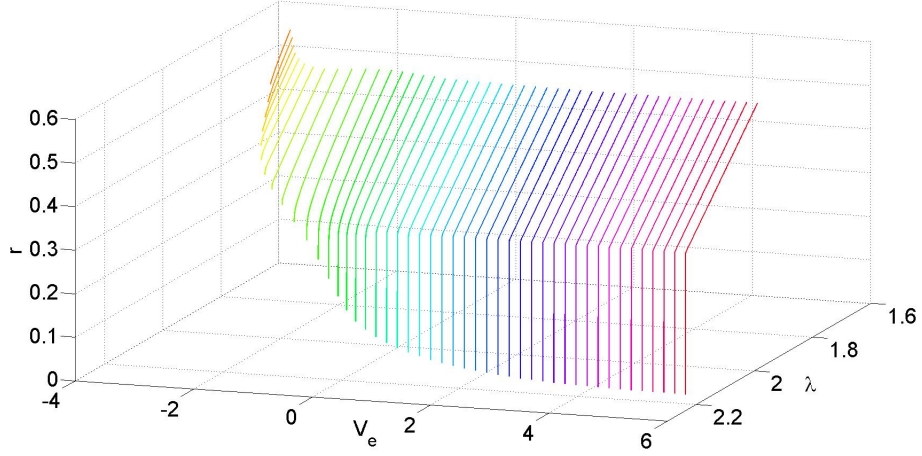


Figure 14: Shock formation in r , as demonstrated by a series of ingoing radial null geodesics in the early phase ($-4 < v_e < 6$) of our numerical simulation. Each line represents $r(\lambda)$ for a single null geodesic (constant v_e value). The gradual development (with increasing v_e) of a sharp break point is clearly seen. The location of this break agrees with the r value of the IH ($r_- \cong 0.35177$). The geodesics are displayed here in a limited range of r ($0 < r \leq 0.6$) in order to improve shock visibility. (Although, geodesics with very small v_e arrive $u = u_{max}$ at r values well above zero.)

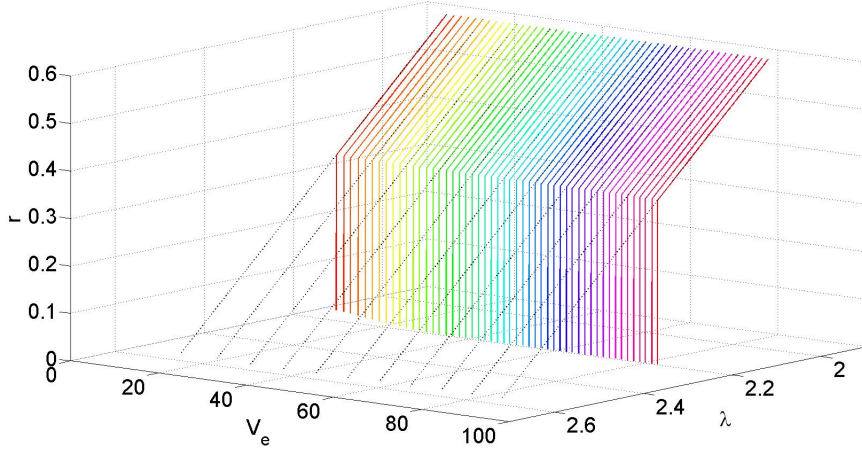


Figure 15: Fully developed shock in r , as demonstrated by a large set of late radial null geodesics (solid colored lines) in the range $10 < v_e < 85.2$. The figure also displays the corresponding set of ingoing null geodesics in the exact RN geometry (dotted black lines). These pure-RN geodesics are given by the linear function $r(\lambda) = r_+ - \lambda$. The geodesics are restricted here to a limited range of r ($0 < r \leq 0.6$) in order to improve shock visibility. In the range $r \gtrsim r_-$ the dotted lines are in fact invisible, because they coincide with the corresponding solid lines (that is, the geodesics in the perturbed spacetime are indistinguishable from their pure-RN counterparts). This situation changes abruptly at the break line at $r \approx r_-$. Beyond that line, at $r \lesssim r_-$, the perturbed-spacetime geodesics suddenly fall (seemingly vertically) towards zero, whereas the RN geodesics continue their straight linear course.

6 DISCUSSION

We numerically confirmed the existence of an effective shock at the left inner-horizon section of a perturbed spherical charged BH, as predicted by Marolf and Ori (MO) [22]. We demonstrated this here for both test scalar-field perturbations and self-gravitating ones. In both cases, the scalar field Φ exhibits an effective shock. In the self-gravitating case, the area coordinate r also exhibits such an effective shock. Since r^2 is a metric function ($= g_{\theta\theta}$), this actually amounts to an (effective) *gravitational shock wave*.²¹

This shock expresses itself as an effective discontinuity in r (or similarly Φ) as a function of proper time τ , along the worldlines of late left-fallers — namely, free-falling observers heading toward the left inner-horizon section. As these left-fallers approach the (would-be) inner horizon, they experience a sudden decrease in r , within an extremely short proper-time interval $\Delta\tau$. Furthermore, this proper-time scale $\Delta\tau$ decreases exponentially with the time of infall into the BH. For delay times (from collapse to jump-in) of typical astrophysical time scales (e.g.) this $\Delta\tau$ becomes tremendously small — smaller than Planckian by many many orders of magnitude.

MO predicted a sharpening rate $\Delta\tau \sim e^{-\kappa v_{eh}}$, where κ is the IH surface gravity of the late-time asymptotic BH, and v_{eh} is the jump-in time expressed in terms of the asymptotic Eddington advanced time v_e . We numerically confirmed this exponential sharpening rate, for both r and Φ .

The analysis by MO [22] mostly concentrated on late-time observers who enter the BH at $v_{eh} \gg M$, after perturbation tails along the EH has decayed. In their discussion they argued, however, that earlier observers should also experience the shock (provided that $v_{eh} \gtrsim$ a few times M). We numerically confirmed this prediction too, as seen in Figs. 3a, 7, and 10a. Our numerical analysis shows the shock development from the early formation stage (relatively small v_{eh}) up to the stage of well-developed shock (at much larger v_{eh}).

In addition to timelike geodesics, we also used null ingoing geodesics to probe the shock (with τ replaced by the affine parameter λ). This method has some advantages, in particular it allows a simpler and more transparent presentation of the effective shock using 3-dimensional graphics.

We would like to emphasize an important property of the shock: As was mentioned above, while v_{eh} increases, the shock width $\Delta\tau$ rapidly decreases. However, apart from this sharpening, the shock amplitude (as well as its internal shape) is insensitive to the increase in v_{eh} . Let's consider the shock in r for concreteness: Very late left-fallers ($v_{eh} \rightarrow \infty$) will experience, enfolded in the shock, a large decrease in r , all the way from r_- down to $r = 0$. This is demonstrated in e.g. Fig. 12 or 15. In particular this implies an unbounded, totally destructive, tidal compression on approaching the (left arm) IH. This should be contrasted with the experience of late *right-fallers*, heading towards the CH: They experience a bounded tidal deformation on approaching the CH; and the magnitude of this deformation typically decreases as an inverse power of v_{eh} , and vanishes as $v_{eh} \rightarrow \infty$.

This research may be extended in several directions. The most obvious extension is to consider some other types of perturbations of spherical charged BHs, and to explore the effective shock formation they induce. Specifically, the addition of null fluids to our numerical code is rather straightforward as it merely involves a minor modification of the constraint equations. MO have not discussed

²¹Although, in this specific case this gravitational shock is not a free-gravity phenomenon, it has been triggered by the scalar field.

null-fluid perturbation specifically; however, their arguments could probably be generalized to this case as well. Note that null fluid is a fairly realistic perturbation as it can well represent (at least to some extent) the accretion of cosmic microwave background (CMB) radiation by the BH. Gravitational and electromagnetic perturbations would also be interesting, but they are considerably harder to numerically analyze (beyond the linear level) because of the inevitable breakdown of spherical symmetry.

The extension of this analysis to *spinning BHs* would be strongly motivated, because realistic astrophysical BHs are expected to be spinning. For instance, in both gravitational-wave events GW150914 [24] and GW151226 [25], the mergers resulted in BHs with significant spins $a/m \sim 0.7$. However, the numerical study of perturbed spinning BHs would probably be much more challenging, due to the lack of spherical symmetry.

In this study, like in Ref. [22], we only considered asymptotically-flat BHs, with perturbations that decay at late time. Hamilton and Avelino [21] pointed out, however, that realistic astrophysical BHs steadily accrete dust as well as CMB photons along cosmological time-scales. It will be interesting to extend the shock analysis to such a situation, where a charged (or spinning) BH accretes for very long times. The null-fluid formulation will presumably be especially useful for this purpose.

Acknowledgments

This research was supported by the Israel Science Foundation (Grant No. 1346/07).

A Numerical solution of the geodesic equation

A.1 Ingoing Radial Timelike Geodesics

We shall process here the geodesic equation and bring it to a form convenient for numerical integration in our numerical code. We begin with the well known covariant form of the geodesic equation:

$$\dot{u}_\alpha = \frac{1}{2} g_{\mu\nu, \alpha} u^\mu u^\nu, \quad (17)$$

where $u_\alpha \equiv g_{\alpha\beta} u^\beta$, an overdot denotes $d/d\tau$, and $u^\mu \equiv \dot{x}^\mu$ (not to be confused with the null coordinate u). Manipulating the right-hand side,

$$g_{\mu\nu, \alpha} u^\mu u^\nu = g_{\mu\nu, \alpha} g^{\mu\varepsilon} u_\varepsilon u^\nu = -g^{\mu\varepsilon}_{, \alpha} g_{\mu\nu} u_\varepsilon u^\nu = -g^{\mu\varepsilon}_{, \alpha} u_\mu u_\varepsilon,$$

we obtain

$$\dot{u}_\alpha = -\frac{1}{2} g^{\mu\nu}_{, \alpha} u_\mu u_\nu. \quad (18)$$

Using the line element (1) we have $-(1/2)g^{uv} = e^{-\sigma}$, and Eq. (18) yields

$$\dot{u}_u = -2e^{-\sigma} u_u u_v \sigma_{, u}, \quad \dot{u}_v = -2e^{-\sigma} u_u u_v \sigma_{, v}. \quad (19)$$

We would like to replace this set by another set in which the independent variable is u (rather than

τ). Hereafter a prime will denote d/du (along the geodesic). Note that $d/du = (u^u)^{-1} d/d\tau$, or more conveniently, $-(1/2)e^\sigma (u_v)^{-1} d/d\tau$. From Eq. (19) we now derive the simple equations for u'_u and u'_v :

$$u'_u = \sigma_{,u} u_u, \quad u'_v = \sigma_{,v} u_u. \quad (20)$$

To complement the set of equations we need the differential equation for $v(u)$ along the geodesic, namely $v' \equiv dv/du = u^v/u^u$, which we rewrite as

$$v' = \frac{u_u}{u_v}. \quad (21)$$

Equations (20) and (21) form a closed set of first-order differential equations for the three unknowns $v(u), u_u(u), u_v(u)$ — provided that $\sigma_{,u}$ and $\sigma_{,v}$ are known functions of u and v . We use standard predictor-corrector scheme in order to propagate the unknowns v, u_u and u_v in u along the geodesics, with finite steps Δu (the same Δu parameter that we use in the numerical simulation of the field equations). The derivatives $\sigma_{,u}$ and $\sigma_{,v}$ are evaluated on the relevant grid points via finite differences, and then second-order interpolated to the geodesic point $v(u)$. Similar second-order interpolation is used in order to evaluate the functions Φ, r, σ (and the mass function m) on the geodesic point once $v(u)$ is known. The proper time τ along the geodesic is found via integration of $d\tau/du = 1/u^u = -(1/2)e^\sigma/u_v$.

A.2 Ingoing Radial Null Geodesics

We begin with the null analog of the covariant-form geodesic equation (17):

$$\dot{k}_\alpha = \frac{1}{2} g_{\mu\nu, \alpha} k^\mu k^\nu, \quad (22)$$

where $k^\mu \equiv dx^\mu/d\lambda$. From the double-null form of the metric (1) it immediately follows that $\dot{k}_\alpha = 0$ for any radial null geodesic (because for each such geodesic only one component is non-vanishing, either k^u or k^v). In particular, for our ingoing radial null geodesics, we get $k_v = \text{const}$ (and k_u vanishes), therefore $du/d\lambda \equiv k^u = \text{const} \cdot g^{uv}$. Inverting this relation, and substituting $1/g^{uv} = g_{uv} = -(1/2)e^\sigma$, we obtain $d\lambda/du = Ce^\sigma$ where C is an arbitrary normalization constant. Thus, along each $v = \text{const}$ geodesic,

$$\lambda(u) = C \int^u e^{\sigma(\tilde{u}, v)} d\tilde{u}. \quad (23)$$

Note that this function $\lambda(u)$ is defined up to two free parameters: the integration constant, and the global normalization constant C .

Numerical implementation: The integration is performed retroactively after σ is known at all grid points along the geodesic. We use a simple integration procedure:

$$\lambda(u + \Delta u) = \lambda(u) + C e^{[\sigma(u, v) + \sigma(u + \Delta u, v)]/2} \Delta u, \quad (24)$$

which is second-order accurate. The parameter C is determined by requiring $d\lambda/dr = -1$ at the EH.

A.2.1 The RN case

Consider now ingoing radial null geodesics in pure RN geometry. When the latter is expressed in the double-null form (1) using Eddington coordinates (u_e, v_e) , one finds $e^\sigma = f(r) \equiv 1 - 2M/r + Q^2/r^2$. The above expression for $d\lambda/du$ then reduces to $d\lambda/du_e = Cf(r)$. Switching from u_e to the tortoise coordinate $r^* = (v_e - u_e)/2$ we get $d\lambda/dr^* = -2Cf(r)$ (recalling that v_e is constant along the ingoing ray). Since r^* satisfies $dr/dr^* = f(r)$, we find that $d\lambda/dr = -2C$. Thus, $\lambda(r)$ is linear along ingoing null geodesics (and the same for outgoing ones).

Again we have two arbitrary constants (C and the integration constant), and as before we choose them such that at the EH λ vanishes and $d\lambda/dr = -1$, obtaining $r(\lambda) = r_+ - \lambda$.

References

- [1] R. Penrose, "Structure of Space-Time" in Battelle Rencontres, edited by C. de Witt and J. Wheeler (W. A. Benjamin, New York, 1968), p. 222.
- [2] M. Simpson and R. Penrose, "Internal Instability in a Reissner-Nordström Black Hole", Int. J. Theor. Phys. **7**, 183 (1973).
- [3] W. A. Hiscock, "Evolution of the interior of a charged black hole", Phys. Lett. **83A**, 110 (1981).
- [4] Y. Gursel, I. D. Novikov, V. D. Sandberg, and A. A. Starobinsky, "Final state of the evolution of the interior of a charged black hole", Phys. Rev. D **20**, 1260 (1979).
- [5] S. Chandrasekhar and J. B. Hartle, "On crossing the Cauchy horizon of a Reissner-Nordström black-hole", Proc. R. Soc. London **A384**, 301 (1982).
- [6] E. Poisson and W. Israel, "Inner-horizon instability and mass inflation in black holes", Phys. Rev. Lett. **63**, 1663 (1989).
- [7] E. Poisson and W. Israel, "Internal structure of black holes", Phys. Rev. D **41**, 1796 (1990).
- [8] A. Ori, "Inner structure of a charged black hole - an exact mass-inflation solution", Phys. Rev. Lett. **67**, 789 (1991).
- [9] M. L. Gnedin and N. Y. Gnedin, "Destruction of the Cauchy horizon in the Reissner-Nordström black hole", Class. Quantum Grav. **10**, 1083 (1993).
- [10] P. R. Brady and J. D. Smith, "Black Hole Singularities: A Numerical Approach", Phys. Rev. Lett., **75**, 1256 (1995).
- [11] L. M. Burko, "Structure of the Black Hole's Cauchy-Horizon Singularity", Phys. Rev. Lett. **79**, 4958 (1997) .

- [12] S. Hod and T. Piran, "Mass Inflation in Dynamical Gravitational Collapse of a Charged Scalar Field", *Phys. Rev. Lett.* **81**, 1554 (1998).
- [13] See e.g. L. M. Burko and A. Ori, "Analytic study of the null singularity inside spherical charged black holes", *Phys. Rev. D* **57**, R7084 (1998).
- [14] F. J. Tipler, "Singularities in conformally at spacetimes", *Phys. Lett.* **64A**, 8 (1977).
- [15] A. Ori, "Strength of curvature singularities", *Phys. Rev. D* **61**, 064016 (2000).
- [16] E. Eilon and A. Ori, "Adaptive gauge method for long-time double-null simulations of spherical black-hole spacetimes", *Phys. Rev. D* **93**, 024016 (2016).
- [17] M. Dafermos, "Stability and Instability of the Cauchy Horizon for the Spherically Symmetric Einstein-Maxwell-Scalar Field Equations", *Ann. Math.* **158**, 875 (2003).
- [18] A. Ori, "Structure of the singularity inside a realistic rotating black hole", *Phys. Rev. Lett.* **68**, 2117 (1992).
- [19] P. R. Brady, S. Droz, and S. M. Morsink, "Late-time singularity inside nonspherical black holes", *Phys. Rev. D* **58**, 084034 (1998).
- [20] A. Ori, "Oscillatory Null Singularity inside Realistic Spinning Black Holes", *Phys. Rev. Lett.* **83**, 5423 (1999).
- [21] For a somewhat different view-point see, however, A. J. S. Hamilton and P. P. Avelino, "The physics of the relativistic counterstreaming instability that drives mass inflation inside black holes", *Phys. Rep.* 495, 1 (2010).
- [22] D. Marolf and A. Ori, "Outgoing gravitational shock wave at the inner horizon: The late-time limit of black hole interiors", *Phys. Rev. D* **86**, 124026 (2012).
- [23] This study by MO [22] was triggered by the picture of extreme black holes at late times suggested in D. Marolf, "The dangers of extremes," *Gen. Rel. Grav.* 42, 2337 (2010). [arXiv:1005.2999 [gr-qc]].
- [24] P. Abbott et al. (LIGO Scientific and Virgo Collaborations), "Observation of Gravitational Waves from a Binary Black Hole Merger", *Phys. Rev. Lett.* **116**, 061102 (2016).
- [25] P. Abbott et al. (Virgo and LIGO Scientific Collaborations), "GW151226: Observation of Gravitational Waves from a 22-Solar-Mass Binary Black Hole Coalescence", *Phys. Rev. Lett.* **116**, 241103 (2016) .